PNAS RESEARCH ARTICLE | EARTH, ATMOSPHERIC, AND PLANETARY SCIENCES

Unexpected anthropogenic emission decreases explain recent atmospheric mercury concentration declines

Aryeh Feinberg[a,1,2], Noelle E. Selin[a,b], Christine F. Braban[c], Kai-Lan Chang[d,e], Danilo Custódio[f], Daniel A. Jaffe[g,h], Katriina Kyllönen[i], Matthew S. Landis[j], Sarah R. Leeson[c], Winston Luke[k], Koketso M. Molepo[l], Marijana Murovec[m], Michelle G. Nerentorp Mastromonaco[n], Katrine Aspmo Pfaffhuber[o], Julian Rüdiger[p], Guey-Rong Sheu[q], and Vincent L. St. Louis[r]

Affiliations are included on p. 9.

Edited by Mark Thiemens, University of California San Diego, La Jolla, CA; received January 30, 2024; accepted September 5, 2024

Anthropogenic activities emit ~2,000 Mg y^{-1} of the toxic pollutant mercury (Hg) into the atmosphere, leading to long-range transport and deposition to remote ecosystems. Global anthropogenic emission inventories report increases in Northern Hemispheric (NH) Hg emissions during the last three decades, in contradiction with the observed decline in atmospheric Hg concentrations at NH measurement stations. Many factors can obscure the link between anthropogenic emissions and atmospheric Hg concentrations, including trends in the reemissions of previously released anthropogenic ("legacy") Hg, atmospheric sink variability, and spatial heterogeneity of monitoring data. Here, we assess the observed trends in gaseous elemental mercury (Hg^0) in the NH and apply biogeochemical box modeling and chemical transport modeling to understand the trend drivers. Using linear mixed effects modeling of observational data from 51 stations, we find negative Hg^0 trends in most NH regions, with an overall trend for 2005 to 2020 of −0.011 ± 0.006 ng m^{-3} y^{-1} (±2 SD). In contrast to existing emission inventories, our modeling analysis suggests that annual NH anthropogenic emissions must have declined by at least 140 Mg between the years 2005 and 2020 to be consistent with observed trends. Faster declines in 95th percentile Hg^0 values than median values in Europe, North America, and East Asian measurement stations corroborate that the likely cause is a decline in nearby anthropogenic emissions rather than background legacy reemissions. Our results are relevant for evaluating the effectiveness of the Minamata Convention on Mercury, demonstrating that existing emission inventories are incompatible with the observed Hg^0 declines.

mercury trends | anthropogenic emissions | atmospheric observations | Minamata Convention on Mercury | chemistry-transport model

Significance

Mercury (Hg) is a global pollutant that bioaccumulates to toxic concentrations along the food chain. Anthropogenic Hg inventories suggest increasing global emissions over recent decades, which is at odds with observed declines of atmospheric Hg concentrations in the Northern Hemisphere (NH). We use statistical and process-based modeling to rule out the possibility that NH anthropogenic emissions of Hg could have increased while atmospheric Hg concentrations declined. This implies that anthropogenic emissions of Hg have very likely declined in recent years. This work informs the effectiveness evaluation of the international Minamata Convention on Mercury. Further research is required to better link emission changes with measured concentrations so that the specific causes of global Hg trends can be identified.

The global Minamata Convention on Mercury is a multilateral environmental agreement that aims to "protect human health and the environment from anthropogenic emissions and releases of mercury," a neurotoxic pollutant (1). As mercury (Hg) is volatile and long lived (~6 mo) in the atmosphere (2), trends in atmospheric mercury concentrations are one of the proposed indicators that will be used to evaluate the Convention's effectiveness (3). However, linking trends in Hg concentrations and anthropogenic emissions is not a straightforward process. The major anthropogenic emission sources of Hg, including artisanal and small-scale gold mining (ASGM), coal combustion, and industrial processes, are distributed heterogeneously across the globe (4, 5). At the same time, legacy reemissions of historical anthropogenic mercury from soils, freshwater, wildfires, and oceans are diffuse background sources, which are thought to make up a larger fraction of the overall Hg source fluxes (60% for legacy reemissions vs. 27% for primary anthropogenic) (6). Atmospheric Hg monitoring stations are also not evenly distributed globally, with more stations located in North America and Europe (7), and they cover different time periods. Therefore, statistical modeling is necessary to maximize the information present in atmospheric Hg records (8), while mechanistic modeling helps connect observed Hg concentrations with their drivers, i.e., emissions, chemical transformations, transport, and deposition (7).

The large-scale trends of atmospheric Hg over the last three decades have been under recent debate. Bottom–up inventories show increasing global anthropogenic emissions since the 1990s (5, 9, 10), which, all else being equal, should increase atmospheric Hg concentrations. However, in North America and Europe, measured gaseous elemental mercury (GEM: Hg^0) concentrations have generally been declining since continuous measurements began in the 1990s (7, 11–14). There is a clear need to understand this contradiction and evaluate past trends of Hg emissions, especially after the adoption of

The authors declare no competing interest.

This article is a PNAS Direct Submission.

[1]To whom correspondence may be addressed. Email: arifeinberg@gmail.com.

[2]Present address: Department of Atmospheric Chemistry and Climate, Institute of Physical Chemistry Blas Cabrera, Spanish National Research Council, Madrid 28006, Spain.

This article contains supporting information online at https://www.pnas.org/lookup/suppl/doi:10.1073/pnas.2401950121/-/DCSupplemental.

Published October 8, 2024.

the Minamata Convention in 2013. Zhang et al. (7), the most recent study to evaluate the consistency between emission inventories and atmospheric observations using the chemical-transport model GEOS-Chem, analyzed available data through 2014. Their comparison between the model and measurements from North America and Europe led the authors to conclude that anthropogenic Hg emissions declined by ~30% between 1990 and 2010 due to weaker increases of Hg emissions from ASGM and strong declines in Hg emissions from commercial products (7). More recent measurements from East Asian stations have also reported declines in atmospheric Hg (15–18). Long-term measurements from the Southern Hemisphere (SH) remain scarce, with the latest results from the observation stations Cape Point and Amsterdam Island showing insignificant trends between 2012 and 2017 (19). Alternative hypotheses have been proposed to explain the decline in atmospheric Hg in the Northern Hemisphere (NH) while anthropogenic emissions rise, including increased elemental mercury (Hg^0) uptake by vegetation (20) and declining Hg emissions from ocean legacy reemissions due to reduced anthropogenic inputs after the 1970s (21, 22). However, a decline in legacy emissions of Hg is difficult to reconcile with biogeochemical box models, which suggest that legacy Hg emissions generally increase if anthropogenic emissions are constant or increasing (23).

Here, we perform trend analyses on a compiled NH dataset (1992 to 2022) of ambient Hg^0 measurements and conduct biogeochemical box model and GEOS-Chem chemistry-transport model simulations to identify emission trends that would be compatible with observed concentration trends. We focus on Hg^0 measurements rather than gaseous oxidized mercury (GOM) and wet deposition measurements, as past measurements of GOM may have been biased low (24) and wet deposition is more strongly affected by meteorological variability (25). We derive trends not only in the mean or median changes in Hg^0 but also in other statistical quantiles (e.g., 95th percentile) using quantile regression, which can provide additional information regarding the drivers of trends.

Results and Discussion

Regional Trends in Observed Hg^0 (1992 to 2022). We analyzed Hg^0 data from 51 long-term monitoring stations across the NH (Fig. 1). To calculate trends over wider regions, we aggregated stations based on Intergovernmental Panel on Climate Change (IPCC) regions (26) and calculated overall trends using linear mixed effect modeling (Fig. 2 *A*–*K* and *SI Appendix*, Table S2). Overall trends for all NH regions except Northwestern North America are declining over the available measurement periods between 1992 and 2022, with declines ranging between –0.007 and –0.035 ng m^{-3} y^{-1} (concentration units refer to standard temperature and pressure, STP). Northwestern North America (Fig. 2*J*) is the only NH region to show a positive trend, but this region only includes one measurement site (Little Fox Lake, Yukon, Canada). Two possible hypotheses for the positive trend in Little Fox Lake have been suggested: increasing transport from East Asia or increasing wildfire frequency in Western Canada (12). However, in our analysis, the East Asian region also shows declining Hg^0 concentrations over 2006 to 2022 (trend –0.023 ± 0.005 ng m^{-3} y^{-1}) (Fig. 2*H*). Declines have also been observed in other published shorter-term measurement records from China (17, 18, 27, 28). For the regions with more available measurement stations, including Eastern North America (ENA, n = 19) and Northern Europe (NEU, n = 13), we tested a nonlinear method of obtaining an overall regional trend using generalized additive models (GAM) (8). The derived regional trends are robust, as both the linear and nonlinear approaches of deriving regional trends yield similar declines in these regions for 2005 to 2020 (–0.01 to –0.02 ng m^{-3} y^{-1}) (*SI Appendix*, Fig. S4).

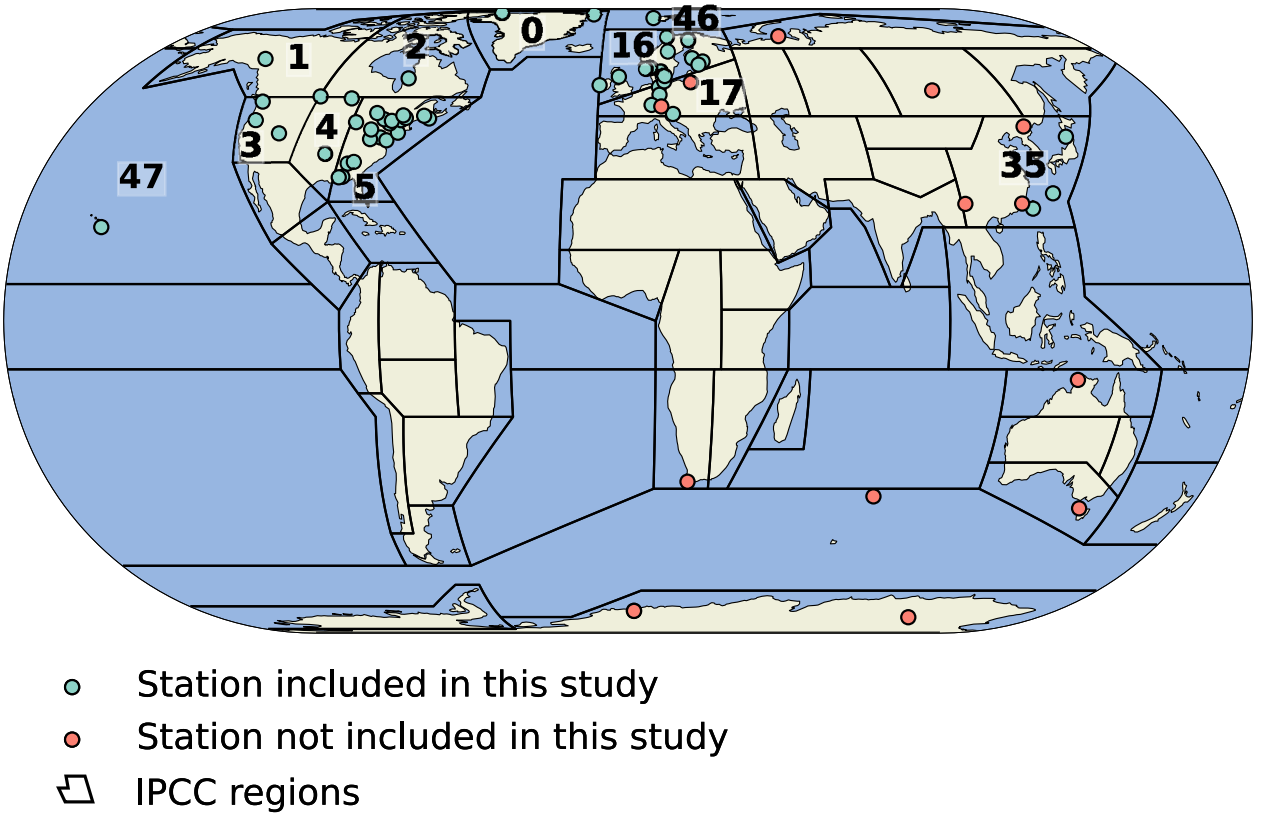

Fig. 1. Map of observation stations that measured atmospheric Hg concentrations for more than 6 y (*SI Appendix*, Table S1). Defined regions (26) are indicated with black lines, with corresponding numbering of included regions listed on the map. For this study, we included NH stations with openly accessible or provided datasets.

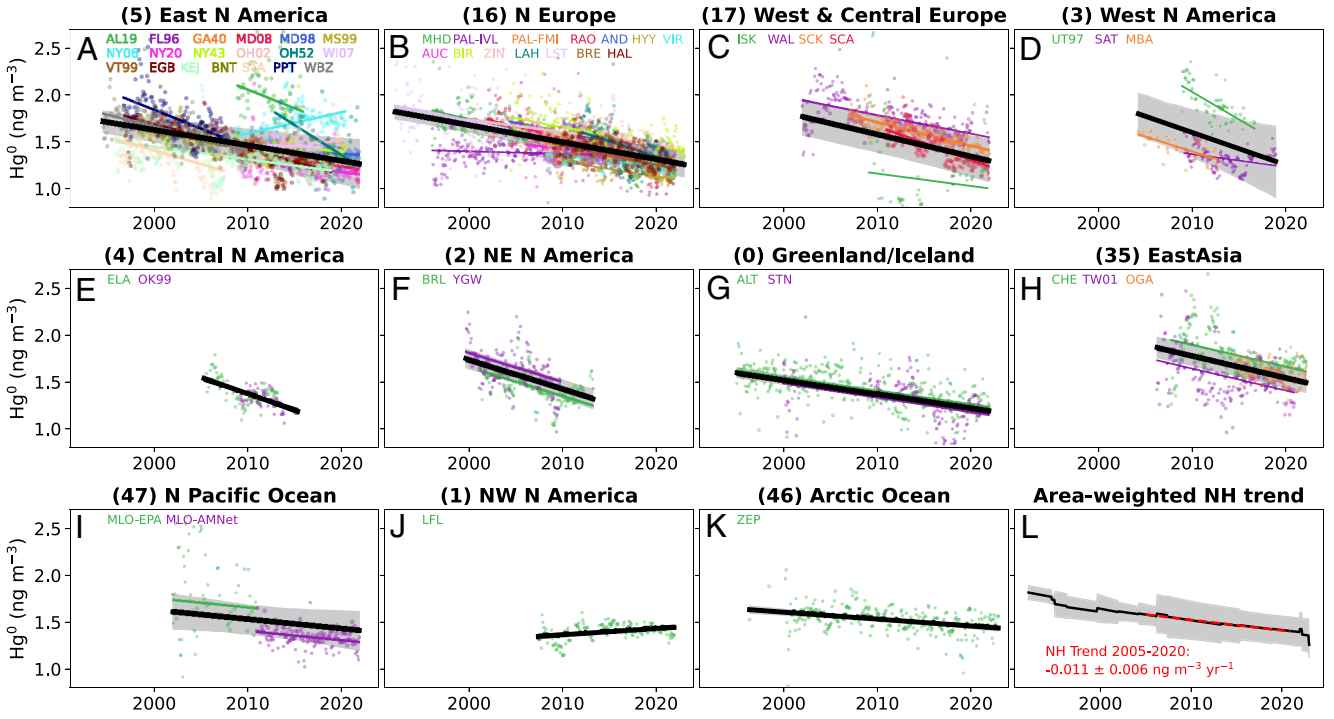

Fig. 2. Trends in observed gaseous elemental mercury (Hg^0) aggregated by the regions (*A*–*K*) in Fig. 1 (labeled by region number). Trends are calculated with linear mixed effects modeling, with overall regional trends shown in black, and shading shows the 5th to 95th percentile range. Individual site deseasonalized monthly means are shown as colored points and individual regressions as colored lines. The overall NH trend (*L*) is calculated by taking the area-weighted average of regional trends, with the shading showing the 2σ averaging error. The red dashed curve in *L* is the linear regression trend for 2005 to 2020, with trend error representing 2σ error from resampling regional trends within their error bounds. We distinguished data from sites where measurements were made by multiple networks, i.e., Pallas (FMI and IVL) and Mauna Loa (EPA and AMNet).

We have also calculated similar regional trends when conducting a sensitivity test where the analysis of site data is limited to the 2005 to 2020 period (*SI Appendix*, Fig. S5 and Table S3).

We find an overall NH Hg^0 decline of –0.011 ± 0.006 ng m^{-3} y^{-1} (±2 SDs) for the period 2005 to 2020 (Fig. 2*L*), calculated by averaging regional trends (Fig. 2 *A*–*K*) weighted by the areas of corresponding IPCC regions. By first aggregating site trends by region, we reduce inherent biases from the uneven spatial distribution of sites (i.e., biasing toward the trends of Eastern North America and Europe) (*SI Appendix*, Fig. S2). Our results largely agree with a previous trend assessment conducted on data from 1990 to 2014 (7), which found regional declines in Hg^0 of –0.6 to –2% y^{-1} (approximately corresponding to –0.01 to –0.03 ng m^{-3} y^{-1}). The current work benefits from improved statistical techniques to combine information from multiple sites and a larger number of stations and regions covered in more recent time periods. We have not included an analysis of SH regional trends in the current work due to the sparse coverage of SH long-term monitoring stations (Fig. 1). From published information, two SH monitoring stations (Cape Point, South Africa, and Amsterdam Island) do not show significant trends during the 2012 to 2017 period, while Cape Point shows a positive trend of ~0.008 ng m^{-3} y^{-1} over 2007 to 2017 (19). As the NH has a wider dataset of Hg^0 time series and is the principal hemisphere for anthropogenic emissions, we proceed with constraining Hg budget trends based on the NH Hg^0 trend.

Constraining Emission Trends for 2005 to 2020. We ran 2 × 10^5 scenarios in a biogeochemical box model for 2005 to 2020, varying 19 Hg budget parameters including the trends in anthropogenic emissions and releases, the response of legacy emissions to recent and historical anthropogenic inputs, emission speciation trends, and the atmospheric Hg lifetime (*SI Appendix*, Table S4). Fig. 3*A* compares the distributions of simulated Hg^0 trends for specific trends in anthropogenic emissions, given the uncertainty ranges of all other factors. Note that emission fluxes are reported in Mg y^{-1}, and thus trends in these fluxes are expressed as Mg y^{-2}. Our best estimate for the observed 2005 to 2020 trend in surface NH Hg^0 is –0.011 ± 0.006 ng m^{-3} y^{-1}. However, to account for potential differences between NH surface and whole troposphere trends (*SI Appendix*, section S3.1), we assumed an extended uncertainty range for NH tropospheric Hg^0 trends from –0.017 to –0.004 ng m^{-3} y^{-1} (error bar in Fig. 3*A*).

The uncertainty range for observed NH troposphere Hg^0 trends is compatible (>5% overlap in the histogram) only with anthropogenic emission trends that are declining by more than –9 Mg y^{-2} (Fig. 3*A*). Stronger declines in anthropogenic emissions lead to more overlap between the simulated and observed trend ranges, yet they become more difficult to reconcile with existing bottom–up inventories. Our box modeling analysis is consistent with a previous emission trend estimate based on 1990 to 2010 observations (610 Mg y^{-1} total difference; –30.5 Mg y^{-2} trend) (7). The positive NH anthropogenic emission trend estimated by the Streets et al. (10) inventory for 2005 to 2015 (34 Mg y^{-2}) should result in NH Hg^0 increases on the order of 0.09 ng m^{-3} y^{-1}, with no overlap in the observed trend range. Other global inventories differ in terms of their temporal coverage, yet the EDGAR v4.tox2 inventory estimates an increase of 54 Mg y^{-2} over 2005 to 2012 in the NH (9) and the AMAP/UNEP inventory estimates an NH increase of 44 Mg y^{-2} between 2010 and 2015 (5). The EDGAR v8.1_toxHg inventory, which was recently released but remains in draft form for speciation estimates (30), shows an NH increase of 35 Mg y^{-2} for 2005 to 2020 (*SI Appendix*, Fig. S15). We conclude that current bottom–up inventories of anthropogenic Hg emissions are inconsistent with the declines in observed NH Hg^0 for 2005 to 2020.

Previous studies (21, 22) have hypothesized that NH Hg^0 may be decreasing due to broad-scale declines in legacy emissions, even as anthropogenic emissions increase or stay constant. However, our

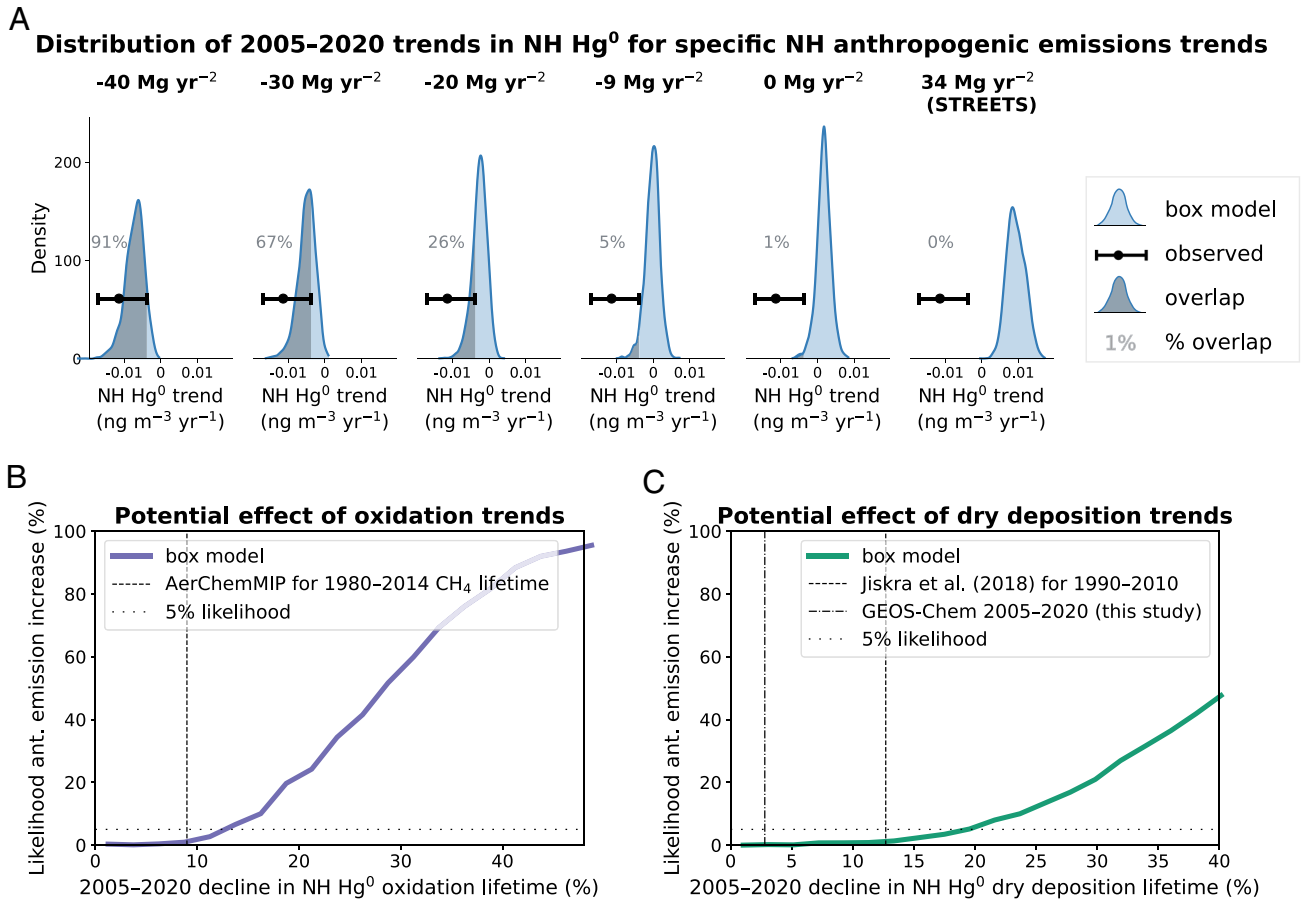

Fig. 3. Modeled relationships between 2005 and 2020 trends in NH Hg^0 concentrations and drivers. (*A*) Histograms showing the relationship between 2005 and 2020 trends in anthropogenic NH emissions and NH Hg^0 trends. We select scenarios with different anthropogenic emission trend values from the 10^5 box model simulations (with a window of ±1 Mg y^{-2} to yield ~2,000 simulations for each trend value). Blue histograms illustrate the probability density of simulated NH Hg^0 trends for each emission trend value. Observed NH Hg^0 trends are shown in the horizontal black line with error bars. The shaded overlap represents the area of the histogram where the model is compatible with observed trends, with the percent of the total area shown in gray. The histogram for the anthropogenic emission trend of 34 Mg y^{-2} represents the Streets et al. (10) 2005 to 2015 trend. (*B*) Impact of NH Hg^0 oxidation lifetime trends on the likelihood of positive anthropogenic (ant.) trends for 2005 to 2020. The *x*-axis shows the relative decline (%) in the NH Hg^0 oxidation lifetime between 2005 and 2020. The *y*-axis refers to the percent of box model runs fitting with the observed NH Hg^0 trend (±2σ) that have positive anthropogenic emission trends. The AerChemMIP (29) estimate for the relative change 1980-2014 methane (CH_4) oxidation lifetime is shown for context. (*C*) Impact of NH Hg^0 dry deposition lifetime on the likelihood of positive anthropogenic (ant.) trends for 2005 to 2020. The *x*-axis shows the relative decline (%) in the NH Hg^0 dry deposition lifetime between 2005 and 2020. The estimated trend in NH dry deposition from ref. 20 for 1990 to 2010 is shown for context, as well as the GEOS-Chem simulated 2005 to 2020 trend (*SI Appendix*, Fig. S11).

biogeochemical box model analysis illustrates that it is very unlikely for legacy emissions to decrease if recent (2005 to 2020) anthropogenic emissions are not also decreasing. Even if anthropogenic emissions stay constant, legacy emissions will grow due to the increasing supply of Hg (23). This effect means that in the case of an anthropogenic emission trend of zero, the median predicted Hg^0 trend will be positive due to positive trends in reemissions (Fig. 3*A* and *SI Appendix*, Fig. S8*B*). The trend in anthropogenic emissions must be below −8 Mg y^{-2} for the median predicted Hg^0 trend to become negative (*SI Appendix*, Fig. S8*B*). We explored the potential impacts of errors in the historical emission and release inventories on the recent reemission trend (*SI Appendix*, Fig. S9). If we assume underestimates in 1970 emissions and releases, when Hg discharges were at their peak (31, 32), the recent reemission trend would be more negative (*SI Appendix*, Fig. S9*A*). However, the degree to which the potential error in 1970 emissions affects the 2005 to 2020 reemission trend is smaller than the impacts of more recent errors (1990, 2000), and a factor of ~15 smaller than the influence of contemporary (2005 to 2020) anthropogenic emission and release trends (*SI Appendix*, Fig. S9 *F* and *G*). Therefore, although historical emissions and releases from earlier decades (>30 y) can affect the recent reemission trend, the dominant factor for the recent reemission trend will be recent trends (<15 y) in anthropogenic Hg inputs to the environment. Our results take into account the uncertainties in the multiple lifetimes of legacy Hg in the surface environment (*SI Appendix*, Table S4).

We explored the role of trend drivers other than anthropogenic inputs by repeating the sampling of the box model throughout the parameter space, accounting for additional causes. If the oxidation lifetime of Hg^0 declined between 2005 and 2020, it can become easier to reconcile the observed Hg^0 decline with positive anthropogenic emission trends (Fig. 3*B*). However, the oxidation lifetime of Hg^0 would have to decline by 13% for at least a 5% likelihood of positive anthropogenic emission trends (i.e., when the oxidation lifetime declines by 13% over 2005 to 2020, 5% of the simulations that are within the observed NH Hg^0 trend range have positive NH anthropogenic emission trends). A hemispheric decrease in the oxidation lifetime of this magnitude would be surprising for the 2005 to 2020 period, as modeling estimates for the methane (CH_4) lifetime suggest only 9% declines over the longer period of 1980 to 2014, driven by increases in hydroxyl radical (OH) concentrations (29). In addition, the two-step Hg oxidation chemistry will be affected by other oxidants as well, including ozone, bromine radicals, and nitrogen oxides (2, 33–35). A recent study has highlighted the role of

Table 1. Description of Hg simulations conducted in GEOS-Chem for 2005 to 2020

Simulation	Anthropogenic emissions	Legacy reemissions	Anthropogenic NH emission trend (Mg y^{-2})	Overall NH emission trend (Mg y^{-2})
BASE	2005 to 2015: Streets et al. (10) 2016 to 2020: repeat 2015	Constant interannually; based on ref. 42	+23	+18
BASE+LEG	2005 to 2015: Streets et al. (10) 2016 to 2020: repeat 2015	Trend from median response to BASE anthropogenic emission trend (*SI Appendix*, Fig. S9*F*)	+23	+31
ZHANG23	2005 to 2020 Chinese emissions from BASE are scaled by emission inventory trend from ref. 45	Trend from median response to ZHANG23 anthropogenic emission trend (*SI Appendix*, Fig. S9*F*)	−11	−12
DEC_ANT_NH	ZHANG23 emissions with additional 23 Mg y^{-2} decrease in anthropogenic emissions spread across NH outside China	Trend from median response to DEC_ANT_NH anthropogenic emission trend (*SI Appendix*, Fig. S9*F*)	−34	−41
DEC_LEG_ONLY	2005 to 2015: Streets et al. (10) 2016 to 2020: repeat 2015	Decline imposed	+23	−30

anthropogenic short-lived halogens in continental Hg oxidation, with more work required to understand their trends (36). Oxidants impacted by anthropogenic pollution sources have likely trended differently in different regions, and therefore are likely not the main factor between the consistent Hg^0 declines seen across the NH. In the unlikely scenario that increased Hg^0 oxidation rates counteracted constant or increasing anthropogenic emissions to yield negative Hg^0 trends, one would still expect to see a positive trend in NH Hg wet deposition. This is because 1) larger emissions would need to be balanced by larger deposition fluxes, and 2) the accelerated oxidation of Hg^0 would lead to more Hg depositing through wet deposition (the major fate of soluble Hg^{II}) rather than dry deposition of Hg^0. However, previous studies have identified overall declines in wet deposition of Hg over North America (13, 14, 37) and Europe (5).

Another potential factor is the increase in terrestrial primary production through global greening, which Jiskra et al. (20) estimated increased the NH dry deposition of Hg^0 to vegetation by 140 Mg y^{-1} between 1990 and 2010; this corresponds to a decrease of approximately 13% in their estimated Hg^0 lifetime due to vegetation uptake. However, the NH Hg^0 dry deposition lifetime would have to decline by more than 19% between 2005 and 2020 to yield a 5% likelihood of positive anthropogenic emission trends (Fig. 3*C*). A change of this magnitude to vegetation uptake during 2005 to 2020 is unrealistic, as our GEOS-Chem simulation for that time period shows only a 3% decline in the Hg^0 dry deposition lifetime due to vegetation changes (*SI Appendix*, Fig. S11). Other climate change factors can play a role in recent legacy emission trends, like release of Hg from melting permafrost (38), changes to ocean evasion of Hg^0 through warming, acidification, and wind speed changes (39), decreased sea ice coverage allowing further Hg^0 evasion (40), and enhanced wildfire emissions (41). These identified climate feedbacks, however, tend to increase legacy Hg reemissions and thus could not explain why anthropogenic emissions in bottom–up inventories increase while Hg^0 trends decline. Although further research into these factors is required to reduce uncertainties in recent trend drivers, our conclusion remains that it is very unlikely that NH anthropogenic emissions could have increased or even stayed constant over 2005 to 2020, with the Hg^0 declines observed over this period in the NH.

Spatial and Quantile Variability of Hg^0 Trends. Although the box model is useful for constraining overall hemispheric trends, it cannot capture the spatial heterogeneity of these trends driven by variability in sources, sinks, and transport. The 3-D chemical-transport model GEOS-Chem (42, 43) is run with observed meteorology from the MERRA-2 reanalysis product (44), meaning that these simulations account for interannual variability or potential climate change-driven trends in meteorology for 2005 to 2020. We ran GEOS-Chem simulations (Table 1) 3-D chemical-transport modelto investigate different emission scenarios over the 2005 to 2020 period and calculated mean trends in NH Hg^0 using area-weighted averaging of observed regions (Fig. 4*A*). The BASE simulation, including anthropogenic emission increases according to Streets et al. (10) for 2005 to 2015 with constant emissions after 2015, shows an increase in NH Hg^0 of 0.006 ng m^{-3} y^{-1}. In the BASE+LEG simulation, we considered the feedback of legacy emissions to increasing anthropogenic emissions, leading to a stronger increase of 0.010 ng m^{-3} y^{-1} in NH Hg^0. Echoing the box modeling results, we thus find that increases in anthropogenic emissions found in existing inventories are inconsistent with the observed trends in NH Hg^0, −0.011 ± 0.006 ng m^{-3} y^{-1}. Replacing Chinese emissions within BASE by the regional inventory trend from ref. 45, the ZHANG23 simulation shows a slight negative trend in NH Hg^0 (−0.001 ng m^{-3} y^{-1}). We simulated two further scenarios for a decreasing NH emission trend: DEC_ANT_NH, where an additional decline of 23 Mg y^{-2} in the NH is imposed on top of the ZHANG23 scenario, and DEC_LEG_ONLY, which considers declining ocean reemissions of Hg in the NH and SH. Both of these emission scenarios are within uncertainties of the observed trend in mean NH Hg^0 (DEC_ANT_NH: −0.009 ng m^{-3} y^{-1}; DEC_LEG_ONLY: −0.012 ng m^{-3} y^{-1}). Since it is difficult to understand the causes of the Hg^0 decline based on the mean hemispheric trend alone, we also assess the spatial and quantile variations in trends.

We use quantile regression to assess trends in the observed median (P50) and 95th percentile (P95) deseasonalized daily Hg^0 values. Fig. 4*B* maps the simulated P50 trends in BASE+LEG, showing increasing concentrations across the globe, in disagreement with 8 of the 9 plotted stations (>13 y observed between 2005 and 2020), which show declines. The difference between P95 trends and P50 trends (Fig. 4*C*) correlates with the change in anthropogenic emissions between 2005 and 2020 (*SI Appendix*, Fig. S12). BASE+LEG simulates P95 declining more than P50 in Eastern North America and Central Europe (areas of emission decreases in the global inventory) and P95 increasing more than P50 in East Asia and South Africa (areas of emission increases). Available high-resolution measurement records confirm the simulated P95–P50 trends in Eastern North America (Egbert and Kejimkujik) and Europe (Mace Head, Schmücke, and Pallas), yet they also show declines in East Asia (Cape

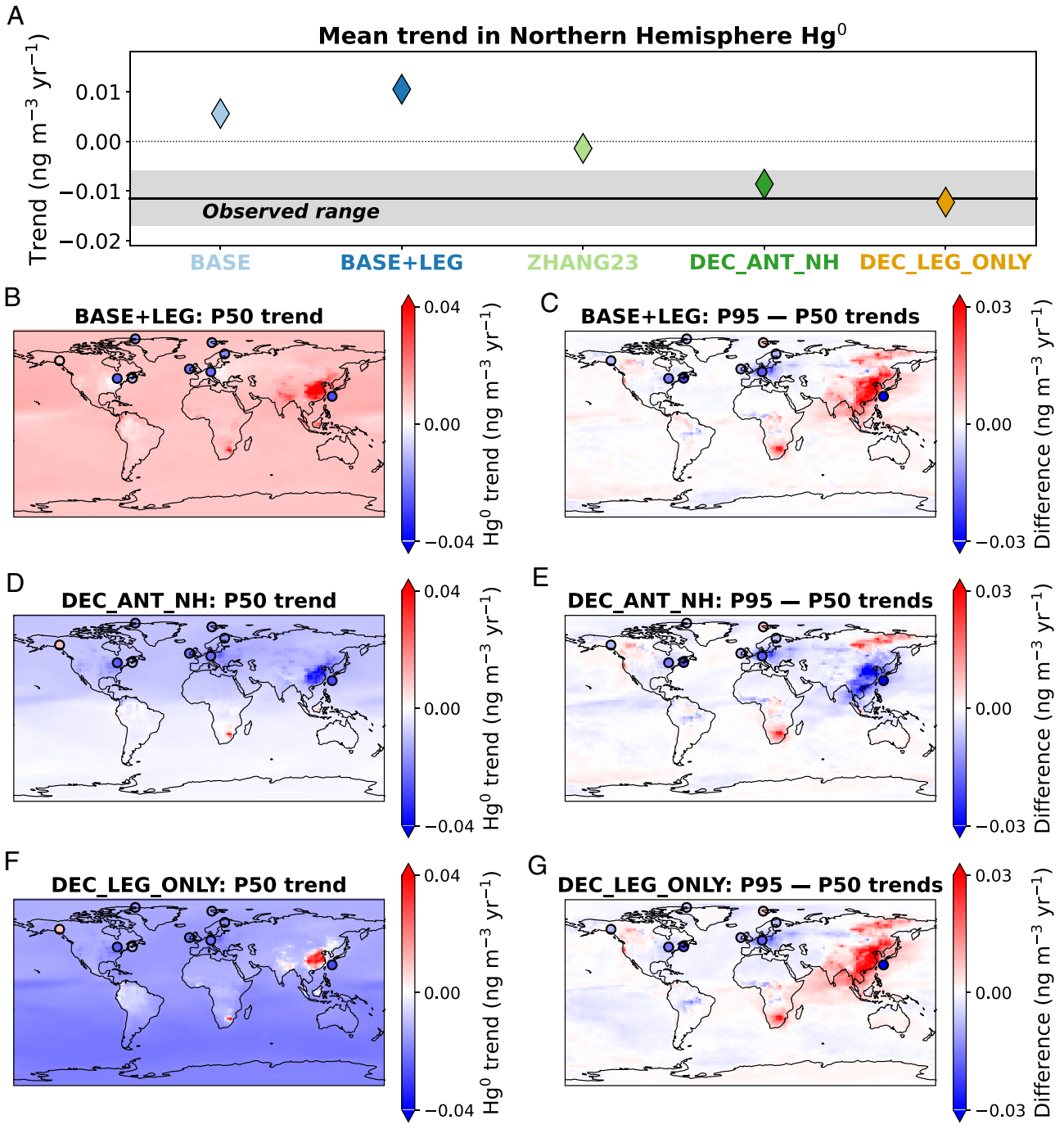

Fig. 4. Comparison between trends (2005 to 2020) in GEOS-Chem model simulations and observations for NH mean Hg^0 (*A*), calculated using linear mixed effects modeling of available NH regions and calculating the area-weighted mean (Fig. 2). The observed range in the NH Hg^0 trend is shown as a black line (mean) with shaded area (±2σ). Error bars are smaller than the markers for the model simulations. Maps show BASE+LEG trends in median (P50) daily deseasonalized simulated values (*B*), BASE+LEG differences between the 95th percentile (P95) trend and median (P50) trend (*C*), DEC_ANT_NH P50 trends (*D*), DEC_ANT_NH differences between P95 and P50 trends (*E*), DEC_LEG_ONLY P50 trends (*F*), DEC_LEG_ONLY differences between P95 and P50 trends (*G*). BASE+LEG is the simulation with Streets et al. (10) emissions and associated legacy feedbacks, DEC_ANT_NH is the simulation with decreasing anthropogenic emissions in the NH, and DEC_LEG_ONLY includes a decline in legacy emissions from the ocean (Table 1). Observed results are plotted in filled circles for 9 stations with more than 13 y of high-frequency data. The other simulations are shown in *SI Appendix*, Fig. S13.

Hedo). In the simulations where Chinese emissions decline between 2005 and 2020 (ZHANG23 and DEC_ANT_NH), the simulated P95–P50 trends agree with observations at Cape Hedo, showing negative values (Fig. 4*E* and *SI Appendix*, Fig. S13*D*). In the DEC_LEG_ONLY simulation, declining legacy emissions lead to agreement with the observed P50 NH Hg^0 trends (Fig. 4*F*), but the P95–P50 trends remain similar to BASE+LEG and are opposite in sign to Cape Hedo observations (Fig. 4*G*). Therefore, despite showing similar P50 trends (Fig. 4 *D* and *F*) in NH Hg^0, DEC_ANT_NH and DEC_LEG_ONLY can be distinguished by simulated patterns in quantile trends. The current results support findings from Hg measurement studies in the 1990s (46, 47), which suggested that reductions in observed extreme concentrations could be useful indicators for regional emission changes. Incorporation of quantile trends as constraints in Hg modeling can thus help maximize the information provided by high-resolution monitoring stations.

Implications for the Drivers of Atmospheric Hg Trends. Observed Hg^0 is generally declining in most NH regions, with an estimated hemispheric trend of –0.011 ± 0.006 ng m^{-3} y^{-1} for 2005 to 2020. By testing a large ensemble of parameters using box modeling and comparing with available measurements of atmospheric concentrations, we showed that NH anthropogenic emissions likely declined by more than –140 Mg y^{-1} (–9 Mg y^{-2}) over this period (Fig. 3*A*). This result is at odds with existing anthropogenic emission inventories (5, 9, 10, 30), which all show NH increases of larger than 34 Mg y^{-2}. Thus, there is a potential gap of 43 Mg y^{-2} (~650 Mg y^{-1}) between estimated anthropogenic emission trends from inventories and trends expected from observed Hg^0 trends. This gap could quantitatively be impacted (in both directions) by factors like the Hg^0 oxidation lifetime and vegetation sink, yet it is unlikely to be substantially reduced (Fig. 3 *B* and *C*). Our ZHANG23 simulation showed that this gap could be partially explained by incorrect Chinese emission trends in the global emission inventory, with Chinese national inventories including more detailed information on air pollution control device efficiencies (45, 48, 49). The hypothesis of declining Chinese emissions is supported by the observed decline in P95 Hg^0 concentrations at Cape Hedo (Fig. 4*E*), along with observed declines in mean Hg^0 values from other East Asian stations (Fig. 2*H*). However, additional declines in anthropogenic emissions across the NH were necessary to match the magnitude of the observed trend in the DEC_ANT_NH simulation. The gap between inventories and measurement-derived emission trends could be due to the large uncertainties associated with several anthropogenic emission sources. For example, ASGM is currently thought to be the largest yet highly uncertain source (globally 775 Mg y^{-1} in 2015) of anthropogenic Hg emissions (10), and estimated trends in this source can differ depending on whether it is estimated to change with time following different proxies such as gold demand or poverty (10, 50). High uncertainties are also linked with emissions from Hg-containing products (globally 436 Mg y^{-1}) (10), as the magnitudes of historically produced Hg are large (~1,000 Gg) and emission factors as well as timescales are uncertain (51). Measurement constraints are limited, and our five tested GEOS-Chem simulations are not intended to cover the entire range of uncertainty in emission scenarios, so we cannot further identify the source types responsible for the discrepancy between emission inventory and observed trends. Nevertheless, both our box and GEOS-Chem modeling analyses suggest that a decline in legacy emissions in the absence of anthropogenic emission reductions is unlikely given our understanding of the Hg cycle and measured quantile trends.

The amount of uncertainty in anthropogenic emissions and biogeochemical cycling of Hg emphasizes the need for continued assessment of inventories and models based on available observations and emerging constraints like Hg isotopes (52). Expansion of current monitoring networks in strategic locations and increased public availability of data would be valuable for trend quantification and attribution to sources. For example, existing SH measurement locations are largely influenced by marine rather than anthropogenic sources (53, 54), with no long-term measurement stations located nearby ASGM activities (Fig. 1). We focused here on trends in Hg^0 in the NH due to the increased prevalence of NH anthropogenic emissions and monitoring, but further monitoring of atmospheric Hg in the SH is essential for constraining trends in Hg sources. For example, major differences between the simulated DEC_ANT_NH and DEC_LEG_ONLY median trends occur in the SH (Fig. 4), but we do not evaluate the accuracy of the simulated SH trends as analysis of SH measurements is out of the scope of the current study. Passive samplers (55) can enable economical Hg monitoring in remote locations, yet active continuous sampling will continue to deliver the benefits of higher time resolution (e.g., atmospheric dynamics, source identification) compared to passive samplers (~monthly resolution). Here, we showed that the trends in the statistical distribution of Hg^0, which can only be facilitated by active sampling methods, are a useful indicator of which sources are changing. As more data become available from sites measuring GOM using methods with smaller biases (56, 57), it will be possible to analyze long-term trends in different fractions of atmospheric Hg, providing further information about source changes. Reduced-form models (58, 59) and tools to produce emission inventories from socioeconomic data more quickly (60), which have been applied extensively in the climate and air pollution fields, can enable more up-to-date evaluations of the latest Hg trends and drivers. Improvements in Hg models will be essential for further analysis of Hg trends, for example refining the response of legacy reemissions to anthropogenic emission scenarios and global change factors. The planned analysis to support the Minamata Convention effectiveness evaluation will advance this approach by investigating the drivers of Hg trends in multiple Hg models (61). As declining atmospheric Hg inputs to ecosystems can directly impact concentrations of Hg in biota (62), understanding the trends in atmospheric Hg burden is essential for better predictions of how Hg pollution will evolve under future regulatory control scenarios and climate change.

Materials and Methods

Atmospheric Mercury Observations. Atmospheric mercury (Hg) occurs as different species: the volatile species gaseous elemental mercury (GEM: Hg^0), the soluble, shorter-lived species GOM (Hg^I and Hg^{II}), and particulate-bound mercury (Hg^P). We compiled data from 51 stations which have more than 6 y of measurements of Hg^0 or total gaseous mercury (TGM = Hg^0 + GOM) in the period 1992 to 2022 (*SI Appendix*, Table S1). Measurements reporting TGM are likely more representative of Hg^0 due to low biases in capturing GOM (63, 64), and therefore we do not differentiate between TGM and Hg^0 measurements. For the main manuscript analysis, we compare modeled Hg^0 quantities to the combined TGM and Hg^0 measurement dataset. As a sensitivity test, we excluded all TGM measurements from the datasets but found no significant differences in regional trends when analyzing Hg^0 measurements alone (*SI Appendix*, Fig. S6 and section S4). We have also tested whether the trend results are similar if modeled TGM data are analyzed instead of modeled Hg^0 and the differences are minor (<0.001 ng m^{-3} y^{-1}). We analyzed data from multiple measurement networks: the US National Atmospheric Deposition Program's (NADP) Atmospheric Mercury Network (AMNet) (65), Environment and Climate Change Canada's network (37), European Monitoring and Evaluation Programme (EMEP) (66), Global Mercury Observation System (GMOS) (67), Ministry of Environment Japan (MOEJ) (15), Ministry of Environment (MOENV) Taiwan (16), and the Experimental Lakes Area (68). We also included a Mauna Loa measurement dataset from the US EPA from 2002 to 2009 (69, 70), which later transitioned into an AMNet site. Most TGM and Hg^0 measurements were made with Tekran Instruments Corporation (Toronto, Canada) Models 2537A/B/X systems, which capture ambient Hg by gold trap amalgamation, subsequently thermally desorbing this accumulated Hg to be detected by cold vapor atomic fluorescence spectrometry (CVAFS) (70). Two sites in the EMEP network (Iskrba after 2017 and Lahemaa) employed Lumex Instruments (St. Petersburg, Russia) Model RA-915 mercury analyzers, which detect Hg^0 through Zeeman atomic absorption spectrometry using high-frequency modulated light polarization (ZAAS-HFM) (71). Before 2017, TGM was measured at Iskrba with Mercury Instruments Analytical Technologies (Karlsfeld, Germany) Model UT-3000 analyzers using cold vapor atomic absorption spectroscopy (CVAAS). All the continuous TGM and Hg^0 measurements are made at 5 to 15 min intervals, which are averaged and reported hourly. Measurements from Zeppelin Station (before 2000), Birkenes (before 2010), Lista, Råö, Bredkälen, Hallahus, and Pallas (the measurements from IVL, Swedish Environmental Research Institute) were made manually with a gold trap sampling technique (72). Data at lower frequencies (manual sites and the Auchencorth Moss and Iskrba timeseries) were used to compute monthly mean statistics for timeseries. At the sites with high-frequency measurements, daily

mean values were calculated and used to compute means for all months with at least 10 d of measurements. All measurement and modeling data for Hg^0 is reported in units of ng m^{-3} y^{-1} at standard temperature and pressure (STP, 0 °C and 1 atm).

Statistical Methods. Monthly mean data were deseasonalized before trend analysis by fitting each station timeseries with four harmonic terms (73). In order to achieve a better evidence synthesis from individual site data, we focused our statistical analysis on calculating overall trends from wider regions. We chose to aggregate Hg trends based on the IPCC regions (Fig. 1). These regions are standardly used in the atmospheric science community and are designed to have consistent climate features (26), providing advantages over using whole continent or country-based aggregations. There are 61 regions in total; we analyzed trends for 11 regions in the NH where stations measuring Hg over the long-term (>6 y) were available. We aim to derive regionally representative trends by integrating information from all data sources because individual sites might only provide a partial view of regional variations, as they cover different time periods, come from different measurement networks, include data gaps, and are potentially exposed to unique local sources and sinks. In previous studies on Hg trends, regional timeseries have been calculated by averaging all sites that are available in a particular year (7). However, this approach is biased when sites do not all cover the same time period since offsets between mean site concentrations can affect the calculated trend results (*SI Appendix*, section S3.2). To address this heterogeneity, we explicitly modeled offsets and trend deviations between sites with linear mixed effects (LME) models (73, 74). Using LME models, a time series can be described with terms representing the consensus trend and intercept for a region ("fixed effect") and terms representing site-level deviations ("random effect"). Individual sites were modeled using Eq. **1**:

$$y_k = a + bt + \alpha_k + \beta_k t, \qquad [1]$$

where y_k are deseasonalized monthly mean Hg^0 values for each site, a is the regional intercept, b is the regional trend, a_k is the site offset, and β_k is the site deviation in trend. To account for autocorrelation, we assumed that residual errors for each site follow a first-order autoregressive process [AR(1)]. We calculated these trends using LME modeling in the R package lme4 (74). For the purposes of LME modeling, EPA and AMNet data for Mauna Loa, as well as Finnish Meteorological Institute (FMI) and Swedish Environmental Research Institute (IVL) data for Pallas, were treated as different sites (as different measurement networks may have offsets). We applied LME modeling to the nine NH regions where multisite data are available. For the two regions (Northwestern North America and the Arctic Ocean) where only one site is available, we calculated generalized least squares (GLS) trends with AR(1) errors on deseasonalized monthly mean values. We chose linear approaches for trend analysis as this follows recommendations for multisite analysis when only a few sites are available for a region (73). We found consistent results between LME trends and nonlinear trends calculated with generalized additive models (GAMs) for regions (Eastern North America and Northern Europe) where a larger number of sites (>12) are available (*SI Appendix*, Fig. S4).

We weighted regional trends by the areas of the corresponding IPCC regions to calculate the overall NH trend, which allowed us to compare with box model simulations. The overall NH trend was calculated for 2005 to 2020, which is the time period with the best availability of data from all 11 regions. The error in the NH trend was calculated through Monte Carlo sampling of regional trends ±2 SD. Analogous trend calculations were performed for GEOS-Chem simulated Hg^0 values, which showed that NH trends derived from regional weighted averages were more representative of the true NH surface trend than averages of all available sites without regional aggregation (*SI Appendix*, Fig. S2).

For sites where high-frequency Hg^0 measurements were available, we additionally calculated quantile regression (QR) trends over the 2005 to 2020 period (75). Other atmospheric chemistry studies (8, 76, 77) have applied QR, as it enables the quantification of trends not only in the mean values but throughout the distribution of the observed quantity. Earlier studies have observed heterogeneous changes in the statistical distribution of atmospheric Hg measurements driven by emission changes (46, 47), yet these have not been followed up with more modern statistical techniques. We analyzed deseasonalized daily mean values at these sites and calculated trends for 5th to 95th percentiles, with errors derived using bootstrapping. We applied the R package quantreg for this analysis (78).

Box Model Simulations. We used a 3-box model that considers atmospheric Hg^0 and Hg^{II} in two tropospheric boxes (NH and SH) and one stratospheric box (79) to simulate potential scenarios for trends during 2005 to 2020. We constructed an ensemble of scenarios accounting for uncertainties in the atmospheric Hg lifetime, historical (pre-2005) anthropogenic emissions and releases, recent (2005 to 2020) anthropogenic emissions and releases, the response of legacy emissions to anthropogenic inputs, and recent (2005 to 2020) speciation trends. We assigned uncertainty ranges to these 19 parameters (*SI Appendix*, Table S4) and sampled 2×10^5 scenarios within this parameter space, using Latin Hypercube Sampling (80).

To address the response in legacy emissions to historical and recent anthropogenic inputs, we applied the effective anthropogenic mercury deposition concept (81). Our approach used two minor adaptations: 1) tracking the effective anthropogenic mercury emissions (EAME) instead of deposition (which leads to offsets of several months in lifetimes); and 2) using a two-term negative exponential model. Given primary emissions or releases of mercury in a specific year (ϵ_i), Eq. **2** calculates the EAME, in a future time t:

$$\mathrm{EAME}_i(t) = \epsilon_i \left(a_1 \exp\left(-\frac{t}{b_1} \right) + a_2 \exp\left(-\frac{t}{b_2} \right) \right), \qquad [2]$$

where a_1 and a_2 are coefficients, and b_1 and b_2 are lifetimes representing the quick and slow reemission processes, respectively. Total legacy emissions (E_{leg}) in the year t were calculated by summing up all EAME_i resulting from previous primary emissions using Eq. **3**:

$$E_{\mathrm{leg}}(t) = \sum_{i<t} \mathrm{EAME}_i. \qquad [3]$$

We employed pulse experiments with parameter perturbations in the Hg Global Biogeochemical Box model (GBC) (6, 82) to calculate reasonable ranges for the a and b parameters (*SI Appendix*, section S5). We pulsed an additional 100 Mg Hg either emitted or released to rivers in 2010 and fit the resultant additional legacy reemissions until 2110 using Eq. **2**. We conducted these pulse experiments on 1,000 iterations of the GBC model, varying each of the 40 rate coefficients and parameters within the GBC model within a factor of 2 using Latin Hypercube Sampling. We found that b_1 ranges between 6 to 15 mo for atmospheric emissions and 2 to 10 mo for releases, corresponding to the timescale of atmospheric deposition and reemission from the surface ocean. The longer lifetime, b_2, ranges between 29 and 97 y for atmospheric emissions and 1 to 117 y for releases, corresponding to the timescale of removal of Hg from the atmosphere–surface ocean–subsurface ocean system through transfer to the deep ocean or temporary storage in soils (6). We calculated ranges for the fraction of Hg reemitted in the short timescale term and the total Hg reemissions resulting from a pulse, which can be used to calculate a_1 and a_2 in Eq. **2**. Although longer time scales (~1,000 y) would be required to model burial of Hg in the deep ocean, Eq. **2** covers the legacy reemission response in near-future projections (<100 y), while having only four parameters as opposed to 40 parameters in the GBC model (81).

Anthropogenic emissions and releases of Hg were taken from the Streets et al. (32) inventory, which covers decadal points over the historical period (1510 to 2010). We accounted for uncertainties in emissions and releases for recent decadal points (1970, 1980, 1990, 2000, 2010) by applying perturbations between –20% and +40% to these values, which is the suggested emission inventory uncertainty range (10). We interpolated between the decadal points to calculate emissions with yearly resolution between 1510 and 2005. For 2005 to 2020, we applied varying linear trends in anthropogenic emissions for both hemispheres, restricting the trend range to ensure non-negative emissions in 2020. The anthropogenic releases for 2005 to 2020 were calculated based on the historical relationship between emission and release trends in the inventory (32), with random perturbations introduced for the hemispheric release trends (*SI Appendix*, Table S4). This procedure yielded 2×10^5 potential timeseries for anthropogenic emissions and releases over 1510 to 2020. Combining these scenarios with varying sets of legacy parameters (Eq. **2**), we calculated the resultant global legacy reemission timeseries for 2005 to 2020 for each of the 2×10^5 scenarios. For simplicity, the distribution of legacy reemissions by hemisphere was assumed to be constant over 2005 to 2020 based on the ratio in GEOS-Chem (44% NH, 55% SH; this is similar to the ratio of ocean coverage in the NH and

SH). Speciation of the anthropogenic emissions in 2005 was set to 65% Hg^0 and 35% Hg^{II}; we applied a variable linear trend in speciation so that speciation in 2020 ranged between 45% and 85% Hg^0.

We ran the 2×10^5 scenarios in the 3-box model for 2005 to evaluate whether the sampled combinations of emissions and atmospheric Hg lifetimes (ranging between 3 and 8 mo) yield a reasonable Hg burden. We rejected scenarios that yield a 2005 burden in the NH troposphere outside of the range 1,600 to 3,300 Mg (corresponding to average tropospheric concentrations of 0.8 to 1.6 ng m^{-3}). Approximately 10^5 samples passed this constraint, which we then utilized for full 2005 to 2020 box model runs. We evaluated linear trends in NH Hg^0 in each of these box model runs and compared these to the inputted total and anthropogenic emission trends for 2005 to 2020.

To assess the impacts of other nonemission factors in NH Hg^0 trends, we repeated this procedure accounting for potential trends in Hg^0 dry deposition and oxidation. We reran the 2×10^5 scenarios with linear trends in the dry deposition rate coefficient so that the value in 2020 varied between 100% and 170% of its value in 2005. Similarly, we ran 2×10^5 scenarios with the Hg^0 oxidation rate coefficient varying in 2020 between 100% and 200% of its value in 2005.

GEOS-Chem Simulations. We ran 3-D atmospheric simulations for the 2005 to 2020 period in the chemistry-transport model GEOS-Chem. We used version 12.8.1 of the Hg model (42) with improvements in the dry deposition of Hg^0 (79). The model was run globally at 2.0° × 2.5° horizontal resolution and 47 vertical levels up to 0.01 hPa (80 km). The model was forced with offline meteorology from the MERRA-2 product (44). The model treats three species of Hg: elemental mercury (Hg^0), oxidized mercury (Hg^{II}, GOM), and particulate mercury (Hg^P). Oxidation of Hg^0 occurs through a two-step mechanism initiated by atomic bromine (Br), while photoreduction of Hg^{II} occurs in the aqueous phase as a function of the NO_2 photolysis rate and organic aerosol concentrations (42). The reduction rate coefficient (K_RED_JNO2) was set to 2.4 m^{-3} μg^{-1} so that modeled Hg^0 concentrations agree with observed values in 2005. The Hg chemistry in GEOS-Chem has been updated in more recent model versions (v14 onward), yet the overall atmospheric lifetime and transport of Hg remain similar (2) and the faster computational speed of v12.8.1 facilitates these 16-y simulations. Legacy reemissions of Hg from the ocean are calculated online (depending on temperature and wind speed) through an air–sea exchange parametrization (83), with concentrations of Hg in the surface ocean taken from a previous ocean general circulation model (MITgcm) simulation (42). Soil legacy emissions are parametrized depending on solar radiation, vegetation cover, and concentrations of Hg in soil (84). The model also considers prompt recycling of Hg^{II} deposited to soils and snow (85), geogenic emissions of Hg^0 (43), and transient emissions of Hg^0 from biomass burning based on GFED v4.1s (86). More comprehensive descriptions of this version of the GEOS-Chem Hg model can be found elsewhere (42, 79).

Five simulations (Table 1) were performed to evaluate spatial heterogeneity in atmospheric Hg trends under different emission scenarios (*SI Appendix*, Fig. S10), which are intended to be illustrative but do not cover the full range of potential scenarios. The BASE case used Streets et al. (10) anthropogenic emissions of Hg for 2005 to 2015, with 2016 to 2020 retaining the same emission pattern as 2015. The BASE+LEG simulation additionally considered the median box modeled trend (*SI Appendix*, Fig. S9*F*) in NH legacy emissions (+14 Mg y^{-2}) due to the BASE trend in NH anthropogenic emissions (+23 Mg y^{-2}) over 2005 to 2020. This trend in legacy emissions was fully ascribed to the ocean through scaling oceanic sea surface concentrations of Hg (42) to yield the NH trend in legacy emissions. In the ZHANG23 scenario, we replaced the trend in Chinese emissions from BASE with the national inventory in ref. 45. To distribute Chinese emissions in a consistent way with the Streets et al. (10) inventory, we scaled the emissions for 2005 to 2020 using the equation:

$$E^{i\prime}_{ZHANG23} = E^{i}_{BASE} \times \frac{E^{i}_{ZHANG23}}{E^{2005}_{ZHANG23}}, \quad [4]$$

where $E^{i\prime}_{ZHANG23}$ are the distributed Chinese emissions applied in the ZHANG23 simulation for year i, E^{i}_{BASE} are the Chinese emissions applied in the BASE, $E^{i}_{ZHANG23}$ are the total Chinese emissions for a specific year in the Zhang et al. (45) inventory, and $E^{2005}_{ZHANG23}$ are the total Chinese emissions in the Zhang et al. (45) inventory for 2005. In this way, the normalized China trend for 2005 to 2020 is taken from ref. 45, but emission magnitudes differ due to differences in 2005 total Chinese emissions between BASE (701 Mg y^{-1}) and ref. 45 (466 Mg y^{-1}). We also adjusted the ZHANG23 trend in NH legacy emissions (+4 Mg y^{-2}) by scaling ocean concentrations so that it is coherent with the NH anthropogenic emission trend (−11 Mg y^{-2}) (*SI Appendix*, Fig. S9*F*).

To develop a scenario with declining anthropogenic emissions that would be compatible with observed NH Hg^0 trends (DEC_ANT_NH), we imposed an additional 23 Mg y^{-2} decline for 2005 to 2020 in the NH. Anthropogenic Hg emissions outside of China were scaled uniformly by year so that the decline is 23 Mg y^{-2} more than in ZHANG23, for a total anthropogenic trend of −34 Mg y^{-2} (Table 1). The NH legacy emissions trend (−2 Mg y^{-2}) was adjusted to be consistent with the DEC_ANT_NH trend in anthropogenic emissions. As a fifth scenario, we explored the possibility where anthropogenic emissions follow BASE, but a major decline (−50 Mg y^{-2}) in NH ocean legacy emissions occurs (DEC_LEG_ONLY). Thus, the mean NH trends in Hg^0 are similar between DEC_ANT_NH and DEC_LEG_ONLY (Fig. 4*A*), but the source contribution and spatial distribution varies. In addition, while DEC_ANT_NH includes stagnant overall SH emissions (−2 Mg y^{-2}), DEC_LEG_ONLY has SH emission declines (−74 Mg y^{-2}) due to the scaling of ocean concentrations.

Data, Materials, and Software Availability. Model code, analysis scripts, and all data to reproduce figures and analyses are published in Zenodo (https://doi.org/10.5281/zenodo.13618039) under a CC BY 4.0 license (https://creativecommons.org/licenses/by/4.0/) (87).

ACKNOWLEDGMENTS. This work was funded by the Swiss NSF through an Early Postdoc.Mobility grant to A.F. (P2EZP2_195424) and a grant (#1924148) from the US NSF to N.E.S. The EPA (https://catalog.data.gov/dataset/epa-sciencehub) through its Office of Research and Development partially funded and contributed to this research. The views expressed in this paper are those of the authors and do not necessarily reflect the views or policies of EPA. It has been subjected to Agency review and approved for publication. Mention of trade names or commercial products does not constitute an endorsement or recommendation for use. We acknowledge Environment and Climate Change Canada (https://www.canada.ca/en/environment-climate-change/services/air-pollution/monitoring-networks-data/canadian-air-precipitation.html), the NADP AMNet (https://nadp.slh.wisc.edu/networks/atmospheric-mercury-network/), New York State Department of Environmental Conservation, EMEP (https://ebas-data.nilu.no), GMOS (https://sdi.iia.cnr.it/gos4m-cat), MOEJ (https://www.env.go.jp/en/chemi/mcm/monitoringdb2.html), MOENV Taiwan, and International Institute for Sustainable Development Experimental Lakes Area (https://www.iisd.org/ela) for the provision of atmospheric mercury data. We would like to acknowledge the following for the funding of the Auchencorth Moss UK site: the UK Department for Environment, Food and Rural Affairs (Defra) and the devolved administrations, via the UK Eutrophying and Acidifying Atmospheric Pollutants contract and by the Natural Environmental Research Council National Capability UK-SCaPE programme (NE/R016429/1). K.-L.C. is supported by NOAA cooperative agreement NA22OAR4320151. We would like to thank David Gay and Ralf Ebinghaus for helpful discussion about available Hg measurements.

Author affiliations: [a]Institute for Data, Systems, and Society, Massachusetts Institute of Technology, Cambridge, MA 02139; [b]Department of Earth, Atmospheric, and Planetary Sciences, Massachusetts Institute of Technology, Cambridge, MA 02139; [c]United Kingdom Centre for Ecology and Hydrology, Penicuik, Midlothian EH26 0QB, United Kingdom; [d]Cooperative Institute for Research in Environmental Sciences, University of Colorado, Boulder, CO 80309; [e]National Oceanic and Atmospheric Administration Chemical Sciences Laboratory, Boulder, CO 80305; [f]Max-Planck-Institut für Biogeochemie, Jena D-07745, Germany; [g]School of Science, Technology, Engineering & Mathematics, Physical Sciences Division, University of Washington Bothell, Bothell, WA 98011; [h]Department of Atmospheric Sciences, University of Washington Seattle, Seattle, WA 98195; [i]Atmospheric Composition Research, Finnish Meteorological Institute, Helsinki 00560, Finland; [j]United States Environmental Protection Agency, Office of Research and Development, Research Triangle Park, NC 27711; [k]National Oceanic and Atmospheric Administration/Air Resources Laboratory, College Park, MD 20740; [l]Institute of Coastal Environmental Chemistry, Helmholtz Zentrum Hereon, Geesthacht 21502, Germany; [m]Slovenian Environment Agency, Environment and Nature protection Office, Air Quality Division, Ljubljana 1000, Slovenia; [n]IVL Swedish Environmental Research Institute, Gothenburg SE-411 33, Sweden; [o]Norwegian Institute for Air Research (NILU), Kjeller 2027, Norway; [p]Air Monitoring Network, German Environment Agency, Langen 63225, Germany; [q]Department of Atmospheric Sciences, National Central University, Taoyuan 320, Taiwan; and [r]Department of Biological Sciences, University of Alberta, Edmonton, AB T6G 2E9, Canada

Author contributions: A.F. and N.E.S. designed research; A.F. performed research; C.F.B., K.-L.C., D.C., D.A.J., K.K., M.S.L., S.R.L., W.L., K.M.M., M.M., M.G.N.M., K.A.P., J.R., G.-R.S., and V.L.S. contributed new reagents/analytic tools; A.F. and N.E.S. analyzed data; N.E.S. supervised research; and A.F. and N.E.S. wrote the paper.

1. UNTC, Minamata Convention on Mercury (2013). https://treaties.un.org/Pages/ViewDetails.aspx?src=TREATY&mtdsg_no=XXVII-17&chapter=27. Accessed 18 September 2024.
2. V. Shah *et al.*, Improved mechanistic model of the atmospheric redox chemistry of mercury. *Environ. Sci. Technol.* **55**, 14445–14456 (2021).
3. UNEP/MC/COP.3, "Proposed indicators for evaluating the effectiveness of the Minamata convention, by article. Annex I to decision MC-3/10" (2020). https://mercuryconvention.org/sites/default/files/documents/decision/UNEP-MC-COP3-Dec10-FirstEffectivenessEvaluation.EN.pdf. Accessed 18 September 2024.
4. F. Steenhuisen, S. J. Wilson, Development and application of an updated geospatial distribution model for gridding 2015 global mercury emissions. *Atmos. Environ.* **211**, 138–150 (2019).
5. UNEP, *Global Mercury Assessment 2018* (UN Environment Programme, Chemicals and Health Branch, Geneva, Switzerland, 2019).
6. H. M. Amos, D. J. Jacob, D. G. Streets, E. M. Sunderland, Legacy impacts of all-time anthropogenic emissions on the global mercury cycle. *Global Biogeochem. Cycles* **27**, 410–421 (2013).
7. Y. Zhang *et al.*, Observed decrease in atmospheric mercury explained by global decline in anthropogenic emissions. *Proc. Natl. Acad. Sci. U.S.A.* **113**, 526–531 (2016).
8. K.-L. Chang *et al.*, Trend detection of atmospheric time series. *Elementa: Sci. Anthropocene* **9**, 00035 (2021).
9. M. Muntean *et al.*, Evaluating EDGARv4.tox2 speciated mercury emissions ex-post scenarios and their impacts on modelled global and regional wet deposition patterns. *Atmos. Environ.* **184**, 56–68 (2018).
10. D. G. Streets *et al.*, Global and regional trends in mercury emissions and concentrations, 2010–2015. *Atmos. Environ.* **201**, 417–427 (2019).
11. D. Custódio *et al.*, Odds and ends of atmospheric mercury in Europe and over the North Atlantic Ocean: Temporal trends of 25 years of measurements. *Atmos. Chem. Phys.* **22**, 3827–3840 (2022).
12. K. MacSween *et al.*, Updated trends for atmospheric mercury in the Arctic: 1995–2018. *Sci. Total Environ.* **837**, 155802 (2022).
13. C. I. Olson, H. Fakhraei, C. T. Driscoll, Mercury emissions, atmospheric concentrations, and wet deposition across the conterminous United States: Changes over 20 years of monitoring. *Environ. Sci. Technol. Lett.* **7**, 376–381 (2020).
14. P. S. Weiss-Penzias *et al.*, Trends in mercury wet deposition and mercury air concentrations across the U.S. and Canada. *Sci. Total Environ.* **568**, 546–556 (2016).
15. K. Marumoto *et al.*, Long-term observation of atmospheric speciated mercury during 2007–2018 at Cape Hedo, Okinawa, Japan. *Atmosphere* **10**, 362 (2019).
16. L. S. P. Nguyen, G.-R. Sheu, D.-W. Lin, N.-H. Lin, Temporal changes in atmospheric mercury concentrations at a background mountain site downwind of the East Asia continent in 2006–2016. *Sci. Total Environ.* **686**, 1049–1056 (2019).
17. J. Shi *et al.*, Measurement report: Atmospheric mercury in a coastal city of Southeast China—Inter-annual variations and influencing factors. *Atmos. Chem. Phys.* **22**, 11187–11202 (2022).
18. Q. Wu *et al.*, Developing a statistical model to explain the observed decline of atmospheric mercury. *Atmos. Environ.* **243**, 117868 (2020).
19. F. Slemr *et al.*, Atmospheric mercury in the Southern Hemisphere—Part 1: Trend and inter-annual variations in atmospheric mercury at Cape Point, South Africa, in 2007–2017, and on Amsterdam Island in 2012–2017. *Atmos. Chem. Phys.* **20**, 7683–7692 (2020).
20. M. Jiskra *et al.*, A vegetation control on seasonal variations in global atmospheric mercury concentrations. *Nat. Geosci.* **11**, 244–250 (2018).
21. F. Slemr, E.-G. Brunke, R. Ebinghaus, J. Kuss, Worldwide trend of atmospheric mercury since 1995. *Atmos. Chem. Phys.* **11**, 4779–4787 (2011).
22. A. L. Soerensen *et al.*, Multi-decadal decline of mercury in the North Atlantic atmosphere explained by changing subsurface seawater concentrations. *Geophys. Res. Lett.* **39**, L21810 (2012).
23. H. Angot *et al.*, Global and local impacts of delayed mercury mitigation efforts. *Environ. Sci. Technol.* **52**, 12968–12977 (2018).
24. S. N. Lyman, L. E. Gratz, S. M. Dunham-Cheatham, M. S. Gustin, A. Luippold, Improvements to the accuracy of atmospheric oxidized mercury measurements. *Environ. Sci. Technol.* **54**, 13379–13388 (2020).
25. A. Giang *et al.*, Understanding factors influencing the detection of mercury policies in modelled Laurentian Great Lakes wet deposition. *Environ. Sci. Process. Impacts* **20**, 1373–1389 (2018).
26. M. Iturbide *et al.*, An update of IPCC climate reference regions for subcontinental analysis of climate model data: Definition and aggregated datasets. *Earth Syst. Sci. Data* **12**, 2959–2970 (2020).
27. Y. Tang *et al.*, Recent decrease trend of atmospheric mercury concentrations in East China: The influence of anthropogenic emissions. *Atmos. Chem. Phys.* **18**, 8279–8291 (2018).
28. P. Sun *et al.*, Declines of gaseous element mercury concentrations at an urban site in eastern China caused by reductions of anthropogenic emission. *Atmos. Environ.* **317**, 120199 (2024).
29. D. S. Stevenson *et al.*, Trends in global tropospheric hydroxyl radical and methane lifetime since 1850 from AerChemMIP. *Atmos. Chem. Phys.* **20**, 12905–12920 (2020).
30. M. Muntean *et al.*, EDGAR v8.1 Global Mercury Emissions. European Commission, Joint Research Centre (JRC) PID (2024). http://data.europa.eu/89h/83b507d7-5218-4dc5-95f9-0ec36f073204. Deposited 19 June 2024.
31. H. Selin, N. E. Selin, From Stockholm to Minamata and beyond: Governing mercury pollution for a more sustainable future. *One Earth* **5**, 1109–1125 (2022).
32. D. G. Streets *et al.*, Five hundred years of anthropogenic mercury: Spatial and temporal release profiles. *Environ. Res. Lett.* **14**, 084004 (2019).
33. T. S. Dibble, H. L. Tetu, Y. Jiao, C. P. Thackray, D. J. Jacob, Modeling the OH-initiated oxidation of mercury in the global atmosphere without violating physical laws. *J. Phys. Chem. A* **124**, 444–453 (2020).
34. J. P. Parrella *et al.*, Tropospheric bromine chemistry: Implications for present and pre-industrial ozone and mercury. *Atmos. Chem. Phys.* **12**, 6723–6740 (2012).
35. A. Saiz-Lopez *et al.*, Photochemistry of oxidized Hg(I) and Hg(II) species suggests missing mercury oxidation in the troposphere. *Proc. Natl. Acad. Sci. U.S.A.* **117**, 30949–30956 (2020).
36. X. Fu *et al.*, Anthropogenic short-lived halogens increase human exposure to mercury contamination due to enhanced mercury oxidation over continents. *Proc. Natl. Acad. Sci. U.S.A.* **121**, e2315058121 (2024).
37. A. Cole *et al.*, A survey of mercury in air and precipitation across Canada: Patterns and trends. *Atmosphere* **5**, 635–668 (2014).
38. K. Schaefer *et al.*, Potential impacts of mercury released from thawing permafrost. *Nat. Commun.* **11**, 4650 (2020).
39. Y. Wang, P. Wu, Y. Zhang, Climate-driven changes of global marine mercury cycles in 2100. *Proc. Natl. Acad. Sci. U.S.A.* **120**, e2202488120 (2023).
40. B. P. DiMento, R. P. Mason, S. Brooks, C. Moore, The impact of sea ice on the air-sea exchange of mercury in the Arctic Ocean. *Deep Sea Res. Part I: Oceanogr. Res. Papers* **144**, 28–38 (2019).
41. A. Kumar, S. Wu, Y. Huang, H. Liao, J. O. Kaplan, Mercury from wildfires: Global emission inventories and sensitivity to 2000–2050 global change. *Atmos. Environ.* **173**, 6–15 (2018).
42. H. M. Horowitz *et al.*, A new mechanism for atmospheric mercury redox chemistry: Implications for the global mercury budget. *Atmos. Chem. Phys.* **17**, 6353–6371 (2017).
43. N. E. Selin *et al.*, Chemical cycling and deposition of atmospheric mercury: Global constraints from observations. *J. Geophys. Res.* **112**, D02308 (2007).
44. R. Gelaro *et al.*, The modern-era retrospective analysis for research and applications, version 2 (MERRA-2). *J. Clim.* **30**, 5419–5454 (2017).
45. Y. Zhang *et al.*, Improved anthropogenic mercury emission inventories for China from 1980 to 2020: Toward more accurate effectiveness evaluation for the Minamata convention. *Environ. Sci. Technol.* **57**, 8660–8670 (2023).
46. Å. Iverfeldt, J. Munthe, C. Brosset, J. Pacyna, "Long-term changes in concentration and deposition of atmospheric mercury over Scandinavia" in *Mercury as a Global Pollutant: Proceedings of the Third International Conference Held in Whistler, British Columbia, July 10–14, 1994*, D. B. Porcella, J. W. Huckabee, B. Wheatley, Eds. (Springer Netherlands, 1995), pp. 227–233.
47. F. Slemr, H. E. Scheel, Trends in atmospheric mercury concentrations at the summit of the Wank mountain, Southern Germany. *Atmos. Environ.* **32**, 845–853 (1998).
48. K. Liu *et al.*, Measure-specific effectiveness of air pollution control on China's atmospheric mercury concentration and deposition during 2013–2017. *Environ. Sci. Technol.* **53**, 8938–8946 (2019).
49. Q. Wu *et al.*, Temporal trend and spatial distribution of speciated atmospheric mercury emissions in China during 1978–2014. *Environ. Sci. Technol.* **50**, 13428–13435 (2016).
50. M. Muntean *et al.*, Trend analysis from 1970 to 2008 and model evaluation of EDGARv4 global gridded anthropogenic mercury emissions. *Sci. Total Environ.* **494–495**, 337–350 (2014).
51. H. M. Horowitz, D. J. Jacob, H. M. Amos, D. G. Streets, E. M. Sunderland, Historical mercury releases from commercial products: Global environmental implications. *Environ. Sci. Technol.* **48**, 10242–10250 (2014).
52. S. Y. Kwon *et al.*, Mercury stable isotopes for monitoring the effectiveness of the Minamata Convention on Mercury. *Earth Sci. Rev.* **203**, 103111 (2020).
53. J. A. Fisher *et al.*, A synthesis of mercury research in the Southern Hemisphere, part 2: Anthropogenic perturbations. *Ambio* **52**, 918–937 (2023).
54. L. Schneider *et al.*, A synthesis of mercury research in the Southern Hemisphere, part 1: Natural processes. *Ambio* **52**, 897–917 (2023).
55. D. S. McLagan *et al.*, A high-precision passive air sampler for gaseous mercury. *Environ. Sci. Technol. Lett.* **3**, 24–29 (2016).
56. S. M. Dunham-Cheatham, S. Lyman, M. S. Gustin, Comparison and calibration of methods for ambient reactive mercury quantification. *Sci. Total Environ.* **856**, 159219 (2023).
57. A. Luippold *et al.*, Use of multiple lines of evidence to understand reactive mercury concentrations and chemistry in Hawai'i, Nevada, Maryland, and Utah, USA. *Environ. Sci. Technol.* **54**, 7922–7931 (2020).
58. F. De Simone *et al.*, A chemical transport model emulator for the interactive evaluation of mercury emission reduction scenarios. *Atmosphere* **11**, 878 (2020).
59. C. W. Tessum, J. D. Hill, J. D. Marshall, InMAP: A model for air pollution interventions. *PLoS One* **12**, e0176131 (2017).
60. W. Atkinson *et al.*, A tool for air pollution scenarios (TAPS v1.0) to enable global, long-term, and flexible study of climate and air quality policies. *Geosci. Model Dev.* **15**, 7767–7789 (2022).
61. A. Dastoor *et al.*, The multi-compartment Hg modeling and analysis project (MCHgMAP): Mercury modeling to support international environmental policy. *Geosci. Model Develop. Discuss.* **2024**, 1–171 (2024).
62. P. J. Blanchfield *et al.*, Experimental evidence for recovery of mercury-contaminated fish populations. *Nature* **601**, 74–78 (2022).
63. A. Steffen *et al.*, A synthesis of atmospheric mercury depletion event chemistry in the atmosphere and snow. *Atmos. Chem. Phys.* **8**, 1445–1482 (2008).
64. M. S. Gustin *et al.*, Do we understand what the mercury speciation instruments are actually measuring? Results of RAMIX. *Environ. Sci. Technol.* **47**, 7295–7306 (2013).
65. D. A. Gay *et al.*, The atmospheric mercury network: Measurement and initial examination of an ongoing atmospheric mercury record across North America. *Atmos. Chem. Phys.* **13**, 11339–11349 (2013).
66. K. Tørseth *et al.*, Introduction to the european monitoring and evaluation programme (EMEP) and observed atmospheric composition change during 1972–2009. *Atmos. Chem. Phys.* **12**, 5447–5481 (2012).
67. F. Sprovieri *et al.*, Atmospheric mercury concentrations observed at ground-based monitoring sites globally distributed in the framework of the GMOS network. *Atmos. Chem. Phys.* **16**, 11915–11935 (2016).
68. V. L. St. Louis *et al.*, Atmospheric concentrations and wet/dry loadings of mercury at the remote experimental Lakes Area, Northwestern Ontario, Canada. *Environ. Sci. Technol.* **53**, 8017–8026 (2019).
69. F. Carbone *et al.*, Sea surface temperature variation linked to elemental mercury concentrations measured on Mauna Loa. *Geophys. Res. Lett.* **43**, 7751–7757 (2016).
70. M. S. Landis, R. K. Stevens, F. Schaedlich, E. M. Prestbo, Development and characterization of an annular denuder methodology for the measurement of divalent inorganic reactive gaseous mercury in ambient air. *Environ. Sci. Technol.* **36**, 3000–3009 (2002).
71. S. Sholupov, S. Pogarev, V. Ryzhov, N. Mashyanov, A. Stroganov, Zeeman atomic absorption spectrometer RA-915+ for direct determination of mercury in air and complex matrix samples. *Fuel Process. Technol.* **85**, 473–485 (2004).
72. Å. Iverfeldt, Occurrence and turnover of atmospheric mercury over the Nordic countries. *Water Air Soil Pollut.* **56**, 251–265 (1991).
73. K.-L. Chang, M. G. Schultz, G. Koren, Niklas Selke, Guidance note on best statistical practices for TOAR analyses. arXiv [Preprint] (2023). https://doi.org/10.48550/arXiv.2304.14236 (Accessed 18 September 2024).
74. D. Bates, M. Mächler, B. Bolker, S. Walker, Fitting linear mixed-effects models using lme4. *J. Stat. Soft.* **67**, 1–48 (2015).
75. R. Koenker, K. F. Hallock, Quantile regression. *J. Econ. Perspect.* **15**, 143–156 (2001).

76. K.-L. Chang *et al.*, Impact of the COVID-19 economic downturn on tropospheric ozone trends: An uncertainty weighted data synthesis for quantifying regional anomalies above Western North America and Europe. *AGU Adv.* **3**, e2021AV000542 (2022).
77. W. C. Porter, C. L. Heald, D. Cooley, B. Russell, Investigating the observed sensitivities of air-quality extremes to meteorological drivers via quantile regression. *Atmos. Chem. Phys.* **15**, 10349–10366 (2015).
78. R. Koenker, quantreg: Quantile regression (2022). https://CRAN.R-project.org/package=quantreg.
79. A. Feinberg, T. Dlamini, M. Jiskra, V. Shah, N. E. Selin, Evaluating atmospheric mercury (Hg) uptake by vegetation in a chemistry-transport model. *Environ. Sci. Process. Impacts* **24**, 1303–1318 (2022).
80. M. D. McKay, R. J. Beckman, W. J. Conover, Comparison of three methods for selecting values of input variables in the analysis of output from a computer code. *Technometrics* **21**, 239–245 (1979).
81. N. E. Selin, A proposed global metric to aid mercury pollution policy. *Science* **360**, 607–609 (2018).
82. H. M. Amos *et al.*, Global biogeochemical implications of mercury discharges from rivers and sediment burial. *Environ. Sci. Technol.* **48**, 9514–9522 (2014).
83. P. D. Nightingale *et al.*, In situ evaluation of air-sea gas exchange parameterizations using novel conservative and volatile tracers. *Global Biogeochem. Cycles* **14**, 373–387 (2000).
84. S. Song *et al.*, Top-down constraints on atmospheric mercury emissions and implications for global biogeochemical cycling. *Atmos. Chem. Phys.* **15**, 7103–7125 (2015).
85. N. E. Selin *et al.*, Global 3-D land-ocean-atmosphere model for mercury: Present-day versus preindustrial cycles and anthropogenic enrichment factors for deposition. *Global Biogeochem. Cycles* **22**, GB2011 (2008).
86. G. R. van der Werf *et al.*, Global fire emissions estimates during 1997–2016. *Earth Syst. Sci. Data* **9**, 697–720 (2017).
87. A. Feinberg, N. E. Selin, Data and code for the publication: "Unexpected anthropogenic emission decreases explain recent atmospheric mercury concentration declines." Zenodo. https://doi.org/10.5281/zenodo.13618039. Deposited 30 August 2024.